ORIGINAL ARTICLE

lajss.org© Latin American Journal of Solids and Structures

www.lajss.org

Sequential Estimation of Bending Rigidity and Prestress Force in Prestressed Concrete Beams Using an Incremental Second-Order-Effect-Guided PINN: A Feasibility Study

Zhanguo Xia[a], **Hong Zhang**[a], **Junkui Pan**[b*]

[a] Henan Quality Institute, No. 23 Middle Yaodian Avenue, Pingdingshan, 467099, China. Email: zhanguoxia_edu@163.com, hongzhangg_edu@163.com

[b] Henan University of Urban Construction, Longxiang Avenue, Pingdingshan, 467036, China. Email: panjk_edu@163.com

* Corresponding author

https://doi.org/10.1590/1679-7825/e9212

Abstract

Prestress force and bending rigidity are coupled in prestressed concrete beams, while prestress-force information is weak in deflection responses. This study proposes an incremental second-order-effect-guided physics-informed neural network (iSOE-PINN) for sequential estimation. A first-order model identifies an equivalent bending rigidity, which is transferred to a second-order PINN for prestress-force estimation. Increasing load scales displacement but does not change the nondimensional axial-force parameter or normalized second-order contribution; any benefit therefore arises from measurement SNR rather than physical decoupling. Independent tests give maximum errors of 0.6% for rigidity and 6.3% for prestress force under 1% Gaussian noise. A 0.26% rigidity-transfer bias predicts an 11.3% prestress-force error, consistent with the sequential result. Across 10 initializations, the mean prestress-force error is 10.89% (SD 0.81 percentage points; 95% CI 10.31%-11.47%). Nine experimental cases yield errors of -3.3% to 3.3% for rigidity and -39.2% to 29.5% for prestress force. The method is therefore a preliminary baseline rather than a field-ready diagnostic tool.

Keywords

prestress-force estimation; bending rigidity; incremental beam-column equation; second-order effect; physics-informed neural networks; sequential inverse analysis

Graphical abstract

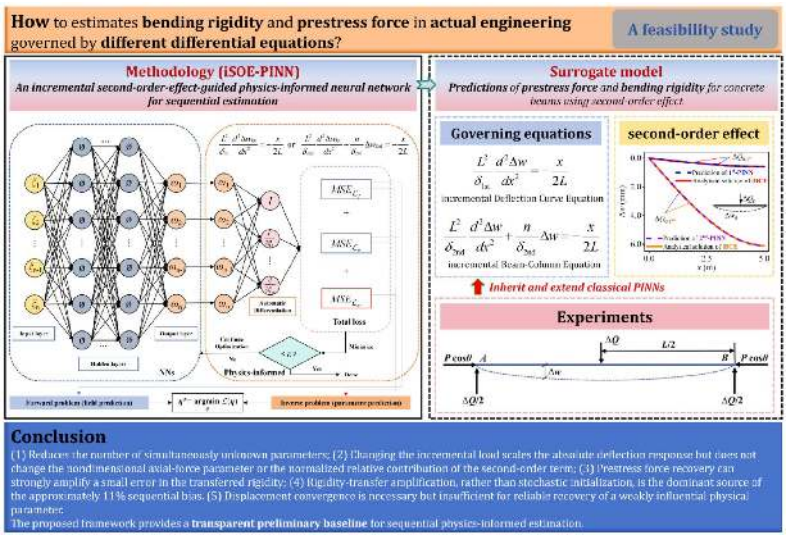

Received July 23, 2026. In revised form August 18, 2026. Accepted September 01, 2026. Available online September 04, 2026.
https://doi.org/10.1590/1679-7825/e9212

Latin American Journal of Solids and Structures. ISSN 1679-7825. Copyright © **2026**. This is an Open Access article distributed under the terms of the Creative Commons Attribution License, which permits unrestricted use, distribution, and reproduction in any medium, provided the original work is properly cited.

1 INTRODUCTION

Background

Prestress force and bending rigidity are two important parameters governing the short-term deformation and service performance of prestressed concrete beams. During service, prestress force may decrease because of concrete creep and shrinkage, prestressing-steel relaxation, and other time-dependent mechanisms. Guo et al. (2018) demonstrated that long-term prestress losses in post-tensioned concrete beams may evolve continuously after construction. The effective bending rigidity of an existing member may also be uncertain because it depends on material properties, cracking, deterioration, and the assumptions adopted in the structural model. Accurate estimation of these parameters is therefore important for structural assessment and maintenance planning, as discussed by Abdel-Jaber and Glisic (2019) and Jia et al. (2023). Nevertheless, prestress force is difficult to infer indirectly because its contribution to common structural responses is generally weaker than the contribution of bending rigidity.

Existing prestress-force assessment methods include direct sensing, vibration-based identification, static-response analysis, finite-element model updating, and data-driven inverse methods. Abdel-Jaber and Glisic (2019) and Jia et al. (2023) reviewed a broad range of direct and indirect techniques for evaluating effective prestress. Direct sensing methods can provide local information but may require embedded or specially installed sensors, limiting their retrospective application to existing structures. Vibration-based approaches use natural frequencies, mode shapes, or other dynamic responses, although these quantities are influenced simultaneously by prestress force, bending rigidity, cracking, mass distribution, boundary conditions, and environmental effects. Breccolotti (2018) investigated prestress-loss assessment using dynamic characteristics, while Huth et al. (2005) examined modal-data-based identification and model updating for a prestressed concrete bridge. Schommer (2017) combined static load testing, sag measurements, modal parameters, and finite-element model updating for bridge assessment. Cornaggia et al. (2023) further investigated inverse parameter identification based on dynamic measurements. Static deflection methods provide a more direct representation of compression-softening effects but generally require accurate displacement measurements and reliable information on bending rigidity, as demonstrated by Bonopera et al. (2018a).

Bonopera et al. (2018a) developed a second-order-deflection method that estimates prestress force from one or more static displacement measurements along a post-tensioned concrete beam. Their formulation is based on Euler-Bernoulli beam theory and requires bending rigidity to be known independently. This requirement is important because uncertainty in bending rigidity is directly transferred to the estimated prestress force. Yang et al. (2025) subsequently introduced an incremental beam-column equation and incorporated it into a PINN framework for prestress-force and bending-rigidity identification. Their study demonstrated the effectiveness of the incremental formulation, particularly when one mechanical parameter is known, while direct identification with multiple unknown parameters remains more demanding.

In recent years, physics-informed neural networks (PINNs) have attracted increasing attention for solving forward and inverse problems governed by differential equations. Raissi et al. (2019) established the widely adopted PINN framework by incorporating governing equations, boundary conditions, and observational data into neural-network training. Lawal et al. (2022) reviewed the subsequent evolution and applications of PINNs, while Toscano et al. (2025) summarized recent developments in physics-informed machine learning. Methodological extensions include the fractional PINN proposed by Pang et al. (2019), the coupled automatic-numerical differentiation strategy developed by Chiu et al. (2022), and the reliability-analysis framework proposed by Meng et al. (2023). Nevertheless, the incorporation of physical equations does not guarantee accurate parameter recovery. Krishnapriyan et al. (2021) demonstrated that PINNs may encounter ill-conditioned optimization, unbalanced loss components, and difficult loss landscapes. Teloli et al. (2025) specifically applied a PINN framework to the identification of displacement, elastic modulus, and damping in beam-like structures. Jeyamohan et al. (2025) proposed a time-domain approach for identifying prestress force and moving force in prestressed concrete bridges using translational and rotational displacement responses.

A direct numerical ranking of these methods is not appropriate because they were developed using different structures, loading conditions, measurement types, unknown parameters, and error definitions (Bonopera et al. 2018b; Dolan and Hamilton 2019; Yapar et al. 2015). The relevant methodological gap is instead that the coupled prestress-force and bending-rigidity problem has not been sufficiently examined as a sequential conditional inverse problem in which information obtained from a reduced first-order model is explicitly transferred to a second-order PINN. Moreover, the approximation error introduced by this transfer requires careful interpretation (Yang et al. 2025; Yu et al. 2022; da Silva and Souza Rosa 2020; Bonopera et al. 2018a).

The present study therefore investigates a sequential framework rather than a strictly decoupled identification method. A first-order PINN is used to estimate a first-order-equivalent bending rigidity, after which a second-order PINN estimates prestress force conditional on the transferred rigidity. Numerical and published experimental data are used to examine both the feasibility and the limitations of this strategy.

Scope and outline

The present study focuses on a slender, uncracked, simply supported prestressed concrete beam subjected to short-term incremental loading. The objective is not to demonstrate exact physical decoupling of bending rigidity and prestress force, but to investigate whether a coupled two-parameter inverse problem can be reorganized into two conditional single-parameter stages.

The main contributions are as follows:

1. A sequential formulation is established by combining a first-order incremental deflection model with a second-order incremental beam-column model. The first stage estimates a first-order-equivalent bending rigidity, and the second stage estimates prestress force conditional on the transferred rigidity.
2. The role of incremental load is clarified. Within the adopted linear incremental model, changing the load magnitude changes the absolute displacement signal but does not change the nondimensional axial-force parameter or the normalized relative contribution of the second-order term.
3. The first- and second-order PINN models are independently verified using analytical solutions, parameter variations, and synthetic measurement noise. The propagation of transferred-rigidity error into prestress-force recovery is then quantified analytically and numerically, and repeated random-initialization tests are used to distinguish systematic transfer amplification from stochastic optimization variability.
4. The framework is applied to nine loading cases reconstructed from a published experimental dataset. The comparison is used to assess feasibility and to examine why convergence of the displacement field is necessary but insufficient for accurate recovery of a weak prestress-force contribution under structural-model and measurement uncertainty.

Section 4 provides numerical verification of the individual models, a representative sequential test, a rigidity-transfer sensitivity analysis, and repeated-initialization statistics. Section 5 applies the method to published experimental beam data and discusses measurement observability, structural-model uncertainty, applicability, and limitations.

2 Methods

Governing equations and assumptions

Once the lateral displacement field is obtained from real-world observations, different mechanical theories can be employed to establish the corresponding analytical models. Based on second-order beam-column theory, Yang et al. proposed the incremental Beam-Column Equation (iBCE), which effectively eliminates long-term effects and further mitigates observation-induced bias (Yang et al. 2025). The governing equation is illustrated in Equation (1) and Figure 1:

$$EI_{2\mathrm{nd}}\frac{d^2\Delta w}{dx^2}+P\Delta w\cos\theta=-\frac{\Delta Q}{2}x \tag{1}$$

where E is Young's elastic modulus, I is the cross-sectional second moment of area; $EI_{2\mathrm{nd}}$ is the second-order bending rigidity; P is the axial compressive prestress force; ΔQ is the incremental load during step loading; x is the axial coordinate of the space; Δw is the deflection increment; and $P\Delta w\cos\vartheta$ is the corresponding second-order moment term.

To characterize second-order effects from a different perspective, an incremental Deflection Curve Equation (iDCE) can also be derived following the same concept. Since the derivation procedure is not original and has been presented in previous studies, only the key steps relevant to the present work are summarized herein. Under the first-order theory, equilibrium is established with respect to the undeformed beam configuration, leading to the following governing equation (Xie et al. 2020):

$$EI_{1\mathrm{st}}\frac{d^2\Delta w}{dx^2}=-\frac{\Delta Q}{2}x \tag{2}$$

where $EI_{1\mathrm{st}}$ denotes the first-order bending rigidity.

Considering a half-span beam at time (t=t_0), the effects of nonhomogeneous terms and initial deflection can be eliminated through incremental analysis. Let W_1 and W_2 denote the total deflections induced by the first loading stage Q_1 and the second loading stage Q_2, respectively, where ΔQ=Q_2-Q_1. The corresponding governing equations can be expressed as

$$\begin{cases} W_1(x,t_0) = w_1(x,t_0) + w_{\mathrm{td}}(x,t_0) \\ W_2(x,t_0) = w_2(x,t_0) + w_{\mathrm{td}}(x,t_0) \end{cases} \tag{3}$$

Subtracting the two equations yields the deflection increment Δ*w* under incremental loading:

$$\Delta w = W_2(x,t_0) - W_1(x,t_0) = w_2(x,t_0) - w_1(x,t_0) \tag{4}$$

Equations (1) and (2) are both second-order linear nonhomogeneous differential equations and exhibit mathematical forms analogous to the classical Beam-Column Equation (BCE). Equation (1) represents the geometric second-order effect through the additional moment term $P\Delta w\cos\vartheta$. For fixed P, EI, and ϑ, however, the incremental differential equation remains linear with respect to the unknown displacement increment Δw. The term "second-order" therefore refers to the geometric equilibrium formulation rather than to a nonlinear differential operator in Δ*w*.

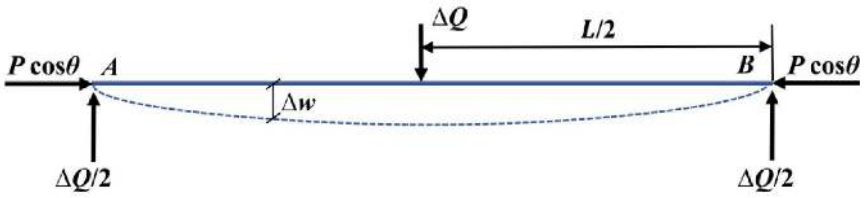

Figure 1 Reference configurations of the iBCE and iDCE models.

The present formulation is based on the following assumptions:

1. the beam is prismatic, slender, initially uncracked, and linearly elastic during each short-term loading increment;
2. the deflection and rotation remain sufficiently small for the adopted incremental beam-column equation;
3. the prestress force remains unchanged between the two measurements used to construct each deflection increment;
4. the supports are represented by ideal simply supported boundary conditions without measurable settlement or rotational restraint;
5. shear deformation, material nonlinearity, tendon slip, three-dimensional effects, and time-dependent deformation during the short measurement interval are neglected.

These assumptions define the applicability of the current Euler-Bernoulli-based formulation. For relatively deep beams or cases in which shear deformation is not negligible compared with the measured deflection increment, a Timoshenko or higher-order beam model is required.

Sequential estimation using first- and second-order models

The first- and second-order incremental equations contain different parameter information. In the first-order formulation, the deflection increment is governed by bending rigidity, whereas the second-order formulation contains both bending rigidity and prestress force. This difference is used to reorganize the coupled inverse problem into two conditional stages.

It is important to distinguish the absolute magnitude of the second-order term from its relative contribution to the governing equation. For fixed structural parameters, the incremental response of the adopted linear model is proportional to the load increment. Let $\Delta w(x)=\Delta Q\bar{w}(x)$ Substitution into Equation (1) gives

$$EI_{2\mathrm{nd}}\frac{d^2\Delta\bar{w}}{dx^2} + P\Delta\bar{w}\cos\theta = -\frac{1}{2}x \tag{5}$$

The load increment Δ*Q* is eliminated from the normalized equation. Therefore, changing Δ*Q* increases or decreases the absolute deflection signal but does not change the relative balance between the bending term and the prestress-force term within the adopted linear model.

In the first stage, the first-order equation is fitted to an observed deflection increment Δw_1. Because the first-order equation omits the term associated with prestress force, the inferred rigidity is interpreted as a first-order-equivalent bending rigidity,

$$EI_{1\mathrm{st}} = \frac{\Delta Q_{1\mathrm{st}} L^3}{\delta_{1\mathrm{st}}} \tag{6}$$

where $\delta_{1\mathrm{st}}$ is identified by the first-order PINN. The quantity $EI_{1\mathrm{st}}$ should not be interpreted as an exact estimate of the bending rigidity appearing in the second-order equation. It may absorb the effect of the omitted geometric-stiffness term as well as measurement and model discrepancies.

In the second stage, the transferred rigidity is treated as fixed conditional information. For a second measured deflection increment Δw_2 and its associated load increment $\Delta Q_{2\mathrm{nd}}$, the characteristic deflection is calculated as

$$\delta_{2\mathrm{nd}} = \frac{\Delta Q_{2\mathrm{nd}} L^3}{EI_{1\mathrm{st}}} \tag{7a}$$

The second-order PINN then identifies the nondimensional axial-force parameter n, from which prestress force is recovered as

$$P = \frac{nEI_{1\mathrm{st}}}{L^2 \cos\theta} \tag{7b}$$

The proposed procedure therefore reduces a coupled two-parameter inverse problem to two conditional single-parameter problems. This reduction can improve optimization tractability, but it does not eliminate the physical dependence between bending rigidity and prestress force. In particular, any bias in $EI_{1\mathrm{st}}$ is transferred to the prestress force estimate in the second stage. The resulting transfer sensitivity is quantified explicitly in Section 4.

The mechanical and measurement roles of the incremental load must be distinguished. Within the adopted linear incremental formulation, the displacement increment can be expressed as $\Delta w(x)=\Delta Q\bar{w}(x)$, whereas the nondimensional axial-force parameter $n=PL^2\cos\vartheta/EI$ is independent of ΔQ. Increasing the load increment therefore provides no intrinsic physical decoupling and does not increase the normalized relative contribution of the second-order term. A different effect may occur at the measurement level. If the displacement sensor has an approximately load-independent absolute noise floor, increasing ΔQ increases the displacement amplitude and can thereby improve the measurement signal-to-noise ratio. By contrast, if measurement uncertainty scales proportionally with response amplitude, increasing ΔQ does not inherently improve the signal-to-noise ratio. The potential experimental benefit of a larger incremental load is therefore a measurement-level effect rather than a change in the governing mechanics.

Nondimensionalization

The objective of nondimensionalization is twofold. First, it establishes a physical system that enables measurements obtained from real structures to be mapped onto the corresponding theoretical model. Second, it alleviates potential multiscale issues during PINN training. In the present problem, bending rigidity EI typically possesses a significantly larger magnitude than other variables and parameters, which may adversely affect the optimization process.

The fundamental distinction between first-order and second-order theories lies in whether geometric nonlinearity is considered through the term $P\Delta w$. To facilitate a unified presentation, all common variables and parameters are expressed using identical symbols whenever possible. In particular, the subscripts “1st” and “2nd” associated with the bending rigidity EI are omitted unless a distinction between the two theories is explicitly required.

The nondimensional variables are defined as

$$\begin{cases} \delta = \dfrac{\Delta Q}{EI} L^3 \\ n = \dfrac{P\cos\theta}{EI} L^2 \\ \xi = \dfrac{x}{L} \\ \Delta\omega = \dfrac{\Delta w}{\delta} \end{cases} \tag{8}$$

which lead to the following relations:

$$\begin{cases} d\xi = \dfrac{dx}{L} \\ d\Delta\omega = \dfrac{d\Delta w}{\delta} \end{cases} \Rightarrow \begin{cases} \dfrac{d\Delta w}{dx} = \dfrac{\delta}{L}\dfrac{d\Delta\omega}{d\xi} \\ \dfrac{d^2\Delta w}{dx^2} = \dfrac{\delta}{L^2}\dfrac{d^2\Delta\omega}{d\xi^2} \end{cases} \tag{9}$$

Substituting Equations (8) and (9) into Equations (1) and (2) yields

$$\begin{aligned} &EI_{1\text{st}}\frac{\delta_{1\text{st}}}{L^2}\frac{d^2\Delta\omega}{d\xi^2} = -\frac{\Delta Q}{2}L\xi \\ &EI_{2\text{nd}}\frac{\delta_{2\text{nd}}}{L^2}\frac{d^2\Delta\omega}{d\xi^2} + P\delta_{2\text{nd}}\Delta\omega = -\frac{\Delta Q}{2}L\xi \end{aligned} \tag{10}$$

After simplification, the governing equations become

$$\frac{d^2\Delta\omega}{d\xi^2} = -\frac{1}{2}\xi \tag{11a}$$

$$\frac{d^2\Delta\omega}{d\xi^2} + n\Delta\omega = -\frac{1}{2}\xi \tag{11b}$$

Equations (11a) and (11b) can be transformed back to their dimensional forms through Equations (8) and (9), thereby establishing the correspondence between the nondimensional physical system and real-world measurements. For example,

$$\begin{cases} \dfrac{d^2\Delta\omega}{d\xi^2} = \dfrac{L^2}{\delta}\dfrac{d^2\Delta w}{dx^2} \\ n\Delta\omega = \dfrac{n}{\delta}\Delta w \\ -\dfrac{1}{2}\xi = -\dfrac{1}{2}\dfrac{x}{L} \end{cases} \tag{12}$$

Finally, we can take

$$\frac{L^2}{\delta_{1\text{st}}}\frac{d^2\Delta w}{dx^2} = -\frac{x}{2L} \tag{13a}$$

$$\frac{L^2}{\delta_{2\mathrm{nd}}}\frac{d^2\Delta w}{dx^2}+\frac{n}{\delta_{2\mathrm{nd}}}\Delta w=-\frac{x}{2L} \tag{13b}$$

The parameter

$$n=\frac{P\cos\theta}{EI}L^2 \tag{14}$$

depends on prestress force, bending rigidity, beam length, and tendon inclination, but not on the incremental load. By contrast, the characteristic deflection

$$\delta=\frac{\Delta Q}{EI}L^3 \tag{15}$$

scales linearly with Δ*Q*. This distinction confirms that changing the load increment modifies the absolute response scale without changing the normalized axial-force parameter.

It should be emphasized that, for both the first- and second-order formulations, the nondimensional deflection increment Δ*ω* in Equations (13a) and (13b) is not directly observable. Instead, it must be obtained indirectly through the measured dimensional deflection increment according to Δ*w*=*δ*Δ*ω*. Therefore, the construction of the PINN framework should be based on observable quantities and measurable physical parameters.

The subsequent PINN-based model is designed to identify the nondimensional parameters *δ* and *n*, from which the corresponding mechanical parameters, namely the prestress force P and the bending rigidity *EI*, can be recovered. The present formulation is limited to loading transitions for which two short-term equilibrium deflection profiles and the corresponding load increment can be determined under an unchanged structural state. Extensions to transient, spatially complex, or nonlinear loading conditions require separate governing equations and are outside the scope of this study.

PINN formulations

The present governing equations are ordinary differential equations in the spatial coordinate *x*. Two PINN models are constructed: the 1st-PINN for the first-order incremental deflection equation and the 2nd-PINN for the second-order incremental beam-column equation.

Let $\Delta\hat{w}_1\left(x;\eta_1\right)$ and $\Delta\hat{w}_2\left(x;\eta_2\right)$ denote the neural-network approximations, where η_1 and η_2 are the trainable network parameters. The physics residuals are written as

$$f_1:=\frac{L^2}{\delta_{1\mathrm{st}}}\frac{d^2\Delta\hat{w}_1}{dx^2}+\frac{x}{2L} \tag{16a}$$

and

$$f_2:=\frac{L^2}{\delta_{2\mathrm{nd}}}\frac{d^2\Delta\hat{w}_2}{dx^2}+\frac{n}{\delta_{2\mathrm{nd}}}\Delta\hat{w}_2+\frac{x}{2L} \tag{16b}$$

For a simply supported half-span model, the boundary conditions are

$$\hat{w}(0)=0,\qquad \frac{d}{dx}\hat{w}\left(\frac{L}{2}\right)=0 \tag{17a}$$

The physics and boundary losses are

$$\mathcal{L}_f=\frac{1}{\mathcal{C}_f}\sum_{x_i\in\mathcal{C}_f}\left|f\left(x_i\right)\right|^2,\qquad \mathcal{L}_b=\frac{1}{\mathcal{C}_b}\sum_{x_i\in\mathcal{C}_b}\left|\mathcal{B}\left[\Delta w\left(x_i\right)\right]\right|^2 \tag{17b}$$

For inverse analysis, measured deflection increments are incorporated through

$$\mathcal{L}_m = \frac{1}{\mathcal{C}_m} \sum_{x_i \in \mathcal{C}_m} \left| \Delta\hat{w}(x_i) - \Delta w_i \right|^2 \tag{18}$$

When a physical parameter in Equations (16a) or (16b) is unknown, it is treated as a trainable scalar and optimized together with the network parameters. The total loss is

$$\mathcal{L} = k_f \mathcal{L}_f + k_b \mathcal{L}_b + k_m \mathcal{L}_m \tag{19}$$

where k_f, k_b and k_m denote the corresponding weights.

In the first stage, δ_1 is optimized together with the network parameters and is subsequently converted into EI_{1st}. In the second stage, δ_2 is fixed using Equation (7a), while n and the second network parameters are optimized. The prestress force is then recovered using Equation (7b).

3 Implementation of the sequential framework

The proposed procedure (Figure 2) requires two short-term loading transitions. For each transition, the total deflection profiles before and after loading are measured and subtracted to obtain a deflection increment. The prestress force and structural condition are assumed to remain unchanged during each short measurement interval.

To reduce architecture-related confounding, the 1st-PINN and 2nd-PINN use the same network depth, width, activation function, floating-point precision, optimizer, collocation-point strategy, and loss weights. Identical configurations do not eliminate stochastic optimization effects, but they provide a consistent basis for comparing the two governing formulations.

To demonstrate the feasibility of the proposed methodology, relatively simple fully connected feed-forward neural networks were consistently adopted throughout this study. Basic hyperparameter settings were employed without introducing additional regularization techniques, such as L_1/L_2 penalties or dropout. A series of numerical examples is presented, together with the available computational settings and a discussion of the corresponding results. Synthetic data generated from the analytical solutions of Equations (22a) and (22b) were treated as observational measurements. All machine-learning procedures were implemented in TensorFlow and executed in Google Colab using an NVIDIA A100 GPU. Parameter optimization was performed using the Adam optimizer.

To assess stochastic optimization stability during revision, an additional repeated-initialization experiment was performed using a fixed fully connected network architecture for all repeated runs. Ten independent neural-network initialization seeds were considered. The physical parameters, observation locations, collocation locations, loss weights, optimizer settings, and initial guesses of the trainable physical scalars were held fixed across runs, while only the neural-network initialization was varied. For each replicate, the independent and sequential 2nd-PINN models were assigned the same paired initialization seed so that their difference was not confounded by different initial network weights. The resulting parameter estimates were summarized using the sample mean, sample standard deviation, and 95% confidence interval.

The optimization procedure of the neural networks is not discussed in detail herein. Interested readers may refer to the literature (Abdolrasol et al. 2021; Abdulkadirov et al. 2023; Zhang 2013) for comprehensive descriptions of the training process. In the present study, the objective is to determine the optimal network parameters η by minimizing the loss function defined in Equation (19). Figure 3 illustrates the modeling framework of the 1st-PINN and 2nd-PINN. As noted previously, both models share the same hyperparameter configuration. Therefore, only one network architecture is presented in Figure 3, despite the fact that the two PINN models are designed for different identification objectives. For clarity, the PINN associated with the iDCE is referred to as the 1st-PINN, whereas the PINN associated with the iBCE is referred to as the 2nd-PINN, thereby explicitly distinguishing the PINN formulations corresponding to the first-order and second-order theories.

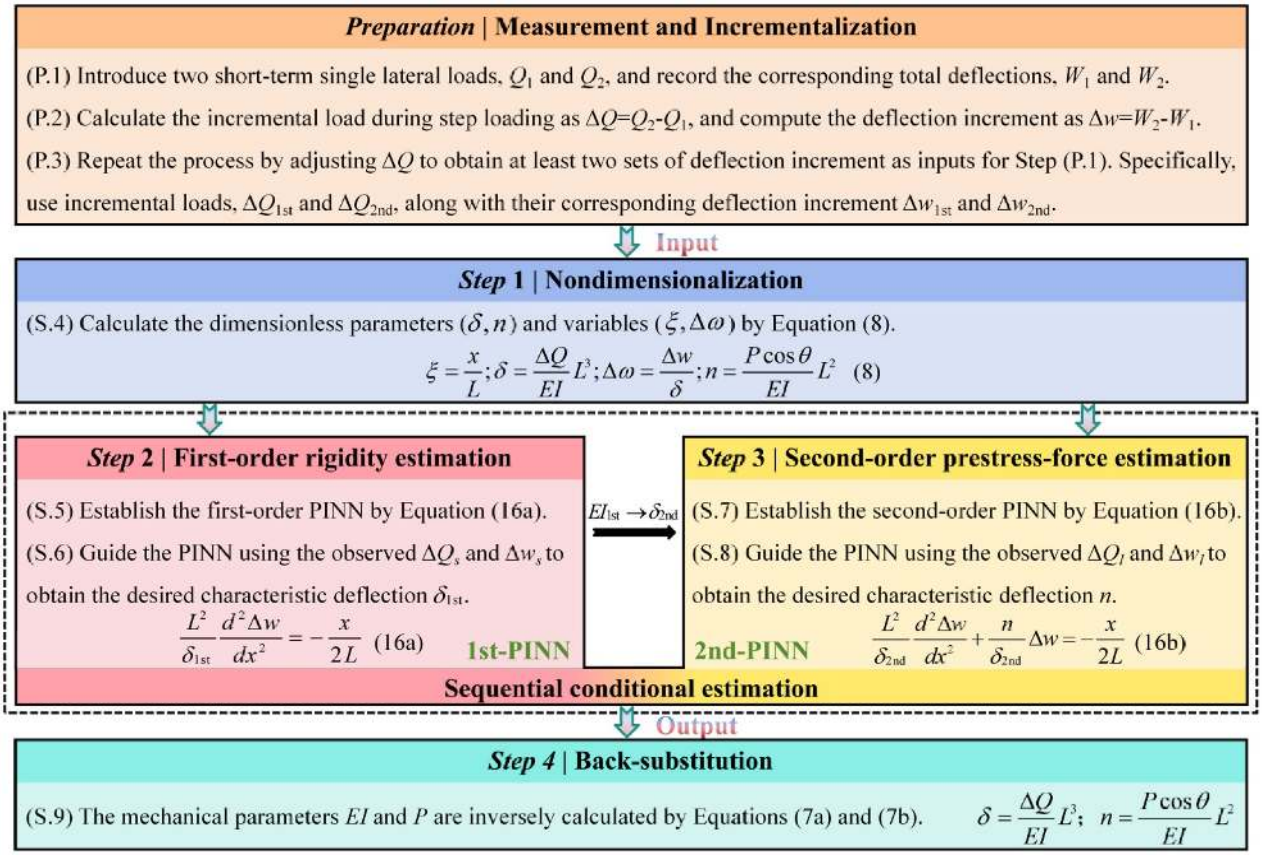

Figure 2 Workflow of parameter identification in prestressed concrete beams.

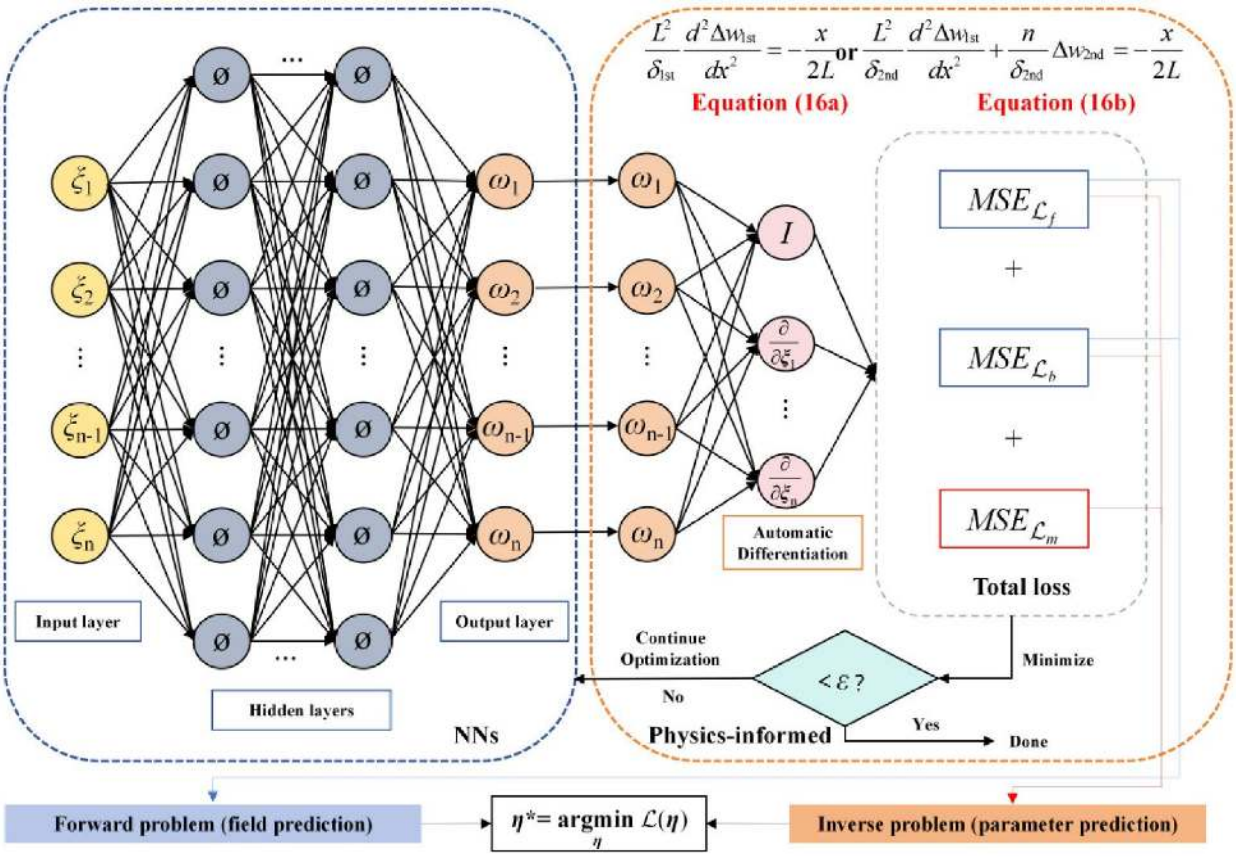

Figure 3 Common neural-network architecture and loss construction used for the 1st-PINN and 2nd-PINN.

4 Numerical verification

Numerical parameter scenarios reported by Yang et al. (2025) were first adopted for independent verification. The sequential framework was subsequently applied to the published experimental deflection data reported by Bonopera et al. (2018a). The corresponding results were compared with those obtained from the analytical solutions given by Equations (22a) and (22b). Based on these comparisons, the rationality and effectiveness of the iSOE-PINN were further assessed for inverse problems involving both single-parameter and multi-parameter identification. The analytical solutions are not treated as competing methods because the governing equations considered in this study admit closed-form solutions. The role of PINN is to provide a unified differentiable framework that can incorporate sparse or noisy observations and trainable physical parameters.

Considering the symmetry of the beam, the general solutions of Equations (16a) and (16b) over the half-span can be expressed as

$$\Delta w_{1\mathrm{st}}\left(x,t_0\right)=-\frac{\Delta Q_{1\mathrm{st}}x^3}{12EI_{1\mathrm{st}}}+Ax+B \tag{20a}$$

and

$$\Delta w_{2\mathrm{nd}}\left(x,t_0\right)=C\cos\mu x+D\sin\mu x-\frac{\Delta Q_{2\mathrm{nd}}}{2P}x \tag{20b}$$

where $\mu^2=P\cos\theta/EI_{2\mathrm{nd}}$. A, B ,C , and D denote the integration constants associated with the corresponding governing equations. After specifying the boundary conditions

$$\Delta w\left(0,t_0\right)=\Delta w'\left(\frac{L}{2},t_0\right)=0 \tag{21}$$

The following deflection increment curve is obtained:

$$\Delta w_{1\mathrm{st}}\left(x,t_0\right)=\frac{\Delta Q_{1\mathrm{st}}x}{48EI_{1\mathrm{st}}}(3L^2-4x^2) \tag{22a}$$

and

$$\Delta w_{2\mathrm{nd}}\left(x,t_0\right)=\frac{\Delta Q_{2\mathrm{nd}}}{2\mu P\cos\theta}\left[\sec\left(\frac{\mu L}{2}\right)\sin\mu x-\mu x\right] \tag{22b}$$

Problem and computational settings

The reference parameters are selected to verify the numerical implementation within the assumed small-deflection and subcritical axial-load regime. They are not intended to represent the full range of prestressed concrete bridge configurations. The reference prestress force satisfies $1.60\times10^6\mathrm{N}=P_0\le0.1P_{cr}=\pi^2EI/L^2\approx6.91\times10^6\mathrm{N}$. The corresponding nondimensional parameters and computational settings are summarized in Tables 1 and 2

Table 1 Mechanical parameter settings during step loading for the independent validation of the 1st-PINN and 2nd-PINN

Number	EI_0 (×10⁸N·m2)		P_0 (×10⁶N)	δ_0		n_0	ΔQ_0 (×10⁴N)		L (m)	
	1st	2nd	2nd	1st	2nd	2nd	1st	2nd	1st	2nd
0	7.00	=1st	1.60	0.0285714286	=1st	0.2285714286	2.00	20.0	10.0	10.0

Table 2 Hyperparameter settings

lr	C_f	kf	C_b	kb	C_m	km
					(Specific to inverse problems)	
0.001	8000	1.00	100	1.00	101	10.0

Forward verification

In the forward tests, prestress force, bending rigidity, load increment, beam length, and tendon inclination are prescribed. The analytical deflection increments are calculated from the corresponding first- and second-order solutions and compared with the PINN predictions.

Figure 4(a) shows close agreement between the analytical and predicted deflection profiles for both formulations. Figure 4(b) presents the corresponding relative L_2 errors during training. The errors decrease rapidly during the initial optimization stage and subsequently fluctuate within a low range.

The two models use the same network and training settings. This consistency reduces, but does not completely eliminate, the influence of architecture and stochastic optimization on their comparison. The results verify that both PINN implementations can reproduce their respective governing equations under the reference settings.

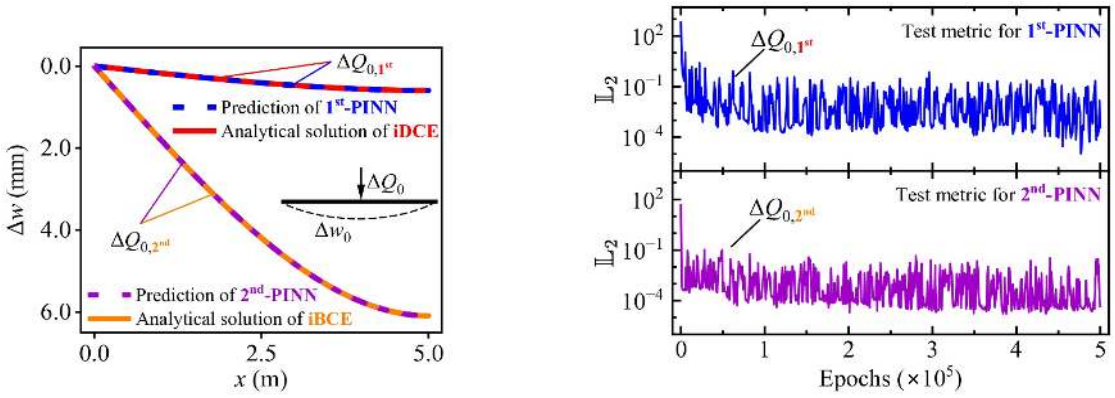

Figure 4 (a) Comparison between analytical solutions and PINN predictions for the independent validation of the 1st-PINN and 2nd-PINN. (b) The relative L_2 error of the 1st-PINN and 2nd-PINN during the independent validation process.

Independent single-parameter inverse verification

Bending rigidity

Figure 5(a) shows the convergence of the characteristic deflection parameter δ in an independent first-order inverse test. The final estimate is $\delta_{0,1st\text{-}PINN}$=0.0284968894, compared with the reference value $\delta_{0,1st=0.0285714286}$. The corresponding signed error is approximately -0.3%. Figure 5(b) shows that the relative displacement error decreases rapidly and remains low after the initial training stage.

This test verifies the ability of the 1st-PINN to identify the parameter appearing in the first-order model. In the sequential framework, the resulting rigidity is interpreted as a first-order-equivalent rigidity. The independent test does not demonstrate that the same value is an exact estimate of the rigidity in the second-order structural model.

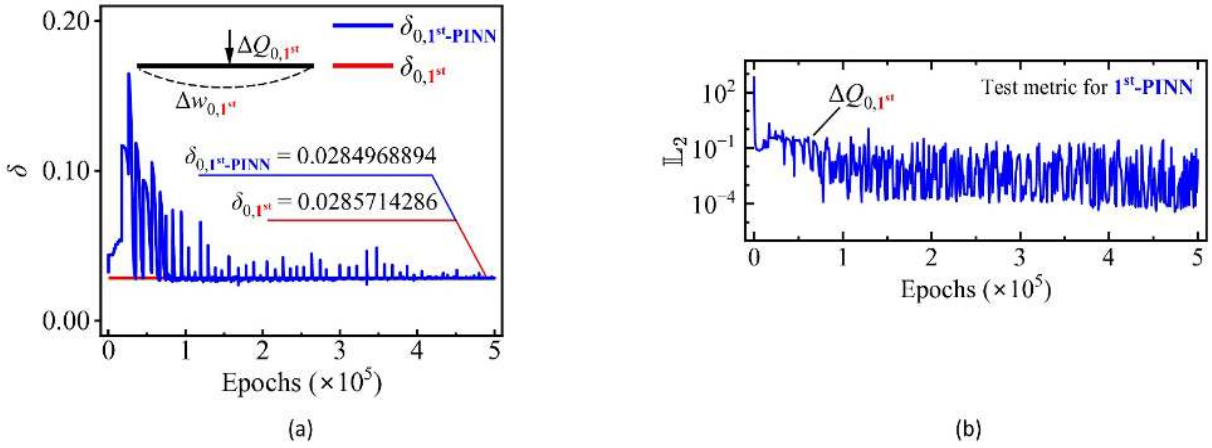

Figure 5 Independent inverse test of the 1st-PINN: (a) convergence of the characteristic deflection parameter δ; (b) relative L2 displacement error.

Prestress force

Figure 6 presents an independent inverse test in which the bending-rigidity-related parameter is prescribed and only the nondimensional axial-force parameter *n* is identified. The estimated value approaches the reference value after an initial transient stage. The corresponding parameter error is approximately -0.2%, while the relative displacement error remains low.

This result verifies the implementation of the 2nd-PINN when the bending-rigidity information is known. It should not be interpreted as a verification of the complete sequential framework because no rigidity-transfer error is present in this independent test.

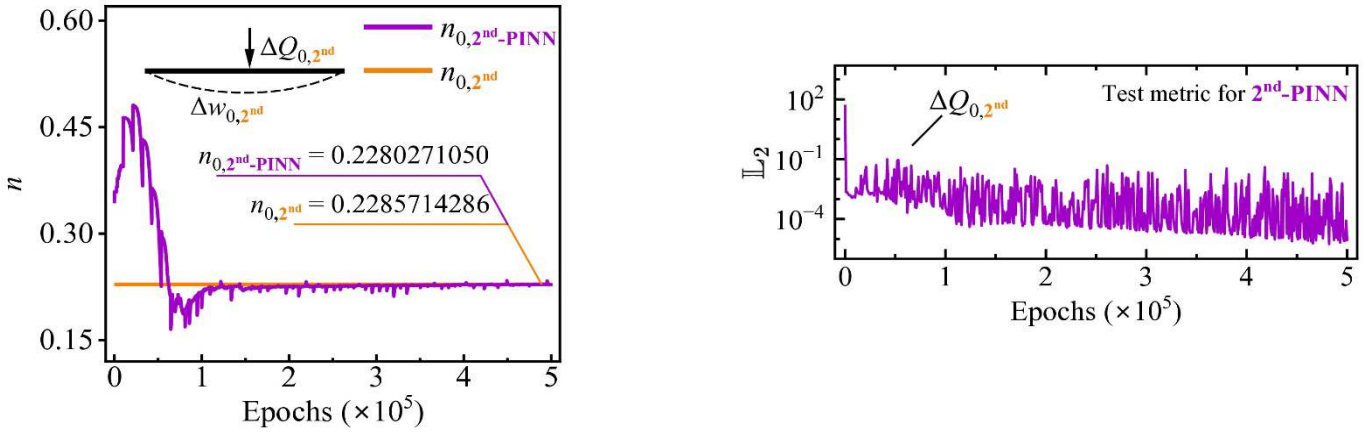

Figure 6 Independent inverse test of the 2nd-PINN: (a) convergence of the nondimensional axial-force parameter n; (b) relative L2 displacement error.

Performance across parameter scenarios and noisy data

Seven independent inverse tests are considered to examine numerical consistency across different parameter settings, and the correct iDCE and iBCE as shown in Table 3. Cases 1[a]–3[a] vary prestress force while maintaining the reference bending rigidity, Cases 4[b]–6[b] vary bending rigidity while maintaining the reference prestress force, and Case 7[c] varies both parameters.

Table 5 presents the results obtained from noise-free synthetic observations. The first-order-equivalent rigidity errors are between approximately -0.2% and 0.1%, while the independently identified prestress-force errors are close to zero for the reported numerical precision.

Table 6 presents the results after adding 1% Gaussian noise to the synthetic observations. The maximum absolute bending-rigidity error is approximately 0.6%, and the maximum absolute prestress-force error is approximately 6.3%. The largest prestress-force error occurs in Case 3[a], in which the reference prestress force is lowest. Under this condition, the response is less sensitive to the axial-force parameter, making its estimation more susceptible to measurement perturbations.

These results demonstrate numerical consistency of the two independently trained PINN models across the considered parameter scenarios. Because a separate model is trained for each case, the tests should not be interpreted as out-of-distribution generalization or extrapolation of a single trained neural network.

Representative sequential estimation

After the two PINN models have been verified independently, a representative synthetic case is used to examine sequential information transfer. The characteristic deflection identified by the 1st-PINN is first converted into the first-order-equivalent rigidity, which is subsequently treated as fixed conditional information in the 2nd-PINN. Figure 7(a) shows the convergence of the nondimensional axial-force parameter. The identified value is $n_{0,\text{iSOE-PINN}}$=0.2531564830, whereas the reference value is $n_{0,2nd}$=0.2285714286, corresponding to an error of approximately 10.8% in *n*. Figure 7(b) shows that the relative displacement error remains low after the initial optimization stage.

Table 3 Correct iDCE and iBCE along with the identified one obtained by learning $\delta_{i,1\mathrm{st}}$, $\delta_{i,2\mathrm{nd}}$, n_i, and Δw.

Correct iDCE	$\frac{L^2}{\delta_{i,1\mathrm{st}}}\frac{d^2\Delta w_{i,1\mathrm{st}}}{dx^2}=-\frac{x}{2L}$
Table 4	
Correct iBCE	$\frac{L^2}{\delta_{i,2\mathrm{nd}}}\frac{d^2\Delta w_{i,2\mathrm{nd}}}{dx^2}+\frac{n_i}{\delta_{i,2\mathrm{nd}}}\Delta w_{i,2\mathrm{nd}}=-\frac{x}{2L}$
Identified iDCE (clean data)	$\frac{L^2}{\delta^{\mathrm{c}}_{i,1\text{st-PINN}}}\frac{d^2\Delta w^{\mathrm{c}}_{i,1\text{st-PINN}}}{dx^2}=-\frac{x}{2L}$
Table 5	
Identified iBCE (clean data)	$\frac{L^2}{\delta^{\mathrm{c}}_{i,2\text{nd-PINN}}}\frac{d^2\Delta w^{\mathrm{c}}_{i,2\text{nd-PINN}}}{dx^2}+\frac{n_i}{\delta^{\mathrm{c}}_{i,2\text{nd-PINN}}}\Delta w^{\mathrm{c}}_{i,2^{\mathrm{nd}}\text{-PINN}}=-\frac{x}{2L}$
Identified iDCE (1% noise)	$\frac{L^2}{\delta^{\mathrm{n}}_{i,1\text{st-PINN}}}\frac{d^2\Delta w^{\mathrm{n}}_{i,1\text{st-PINN}}}{dx^2}=-\frac{x}{2L}$
Table 6	
Identified iBCE (1% noise)	$\frac{L^2}{\delta^{\mathrm{n}}_{i,2\text{nd-PINN}}}\frac{d^2\Delta w^{\mathrm{n}}_{i,2\text{nd-PINN}}}{dx^2}+\frac{n_i}{\delta^{\mathrm{n}}_{i,2\text{nd-PINN}}}\Delta w^{\mathrm{n}}_{i,2\text{nd-PINN}}=-\frac{x}{2L}$

Table 4 Mechanical parameter settings for the independent validation of the 1st-PINN and 2nd-PINN.

Cases (N_i)	EI_i (×10⁸N·m²)		P_i (×10⁶N)	δ_i		n_i	ΔQ_i (×10⁴N)		Loss (%)	
	1st	2nd	2nd	1st	2nd	2nd	1st	2nd	EI_i / EI_0	P_i / P_0
1[a]	7.00	=1st	1.44	0.0285714286	=1st	0.2057142857	2.00	20.0	0.00	10.0
2[a]	7.00	=1st	1.28	0.0285714286	=1st	0.1828571429	2.00	20.0	0.00	20.0
3[a]	7.00	=1st	0.96	0.0285714286	=1st	0.1371428571	2.00	20.0	0.00	40.0
4[b]	6.65	=1st	1.60	0.0300751880	=1st	0.2406015038	2.00	20.0	5.00	0.00
5[b]	6.30	=1st	1.60	0.0317460317	=1st	0.2539682540	2.00	20.0	10.0	0.00
6[b]	5.60	=1st	1.60	0.0357142857	=1st	0.2857142857	2.00	20.0	20.0	0.00
7[c]	5.60	=1st	0.96	0.0357142857	=1st	0.1714285714	2.00	20.0	20.0	40.0

Table 5 The identification results and percentage errors for the seven test cases with clean data

Cases (N_i)	EI_i^{c} (×10⁸N·m²)	P_i^{c} (×10⁶N)	δ_i^{c}	n_i^{c}	L_2		Error (%)	
	1st-PINN	2nd-PINN	1st-PINN	2nd-PINN	1st-PINN	2nd-PINN	$EI^{\mathrm{c}}_{i,1\text{st-PINN}}$ / $EI_{i,1\mathrm{st}}$	$P^{\mathrm{c}}_{i,2\text{nd-PINN}}$ / $P_{i,2\mathrm{nd}}$
1[a]	7.01	1.44	0.0285210684	0.2052171831	6.75E-04	1.11E-05	**0.14**	**0.00**
2[a]	7.01	1.28	0.0285473280	0.1823845209	1.08E-04	9.37E-06	**0.14**	**0.00**
3[a]	7.01	0.96	0.0285506677	0.1365806757	3.32E-05	9.93E-06	**0.14**	**0.00**
4[b]	6.64	1.60	0.0301023182	0.2402223652	6.20E-05	2.12E-05	**-0.15**	**0.00**
5[b]	6.30	1.60	0.0317307822	0.2535141707	5.23E-05	8.13E-06	**0.00**	**0.00**
6[b]	5.60	1.60	0.0357011035	0.2857977748	4.53E-05	6.55E-06	**0.00**	**0.00**
7[c]	5.60	0.96	0.0357023962	0.1707837876	3.92E-05	1.04E-05	**0.00**	**0.00**

Table 6 The identification results and percentage errors for the seven test cases with 1% noise data

Cases (N_i)	EI_i^n (×10⁸N·m²)	P_i^n (×10⁶N)	δ_i^n	n_i^n	L_2		Error (%)	
	1st-PINN	2nd-PINN	1st-PINN	2nd-PINN	1st-PINN	2nd-PINN	$EI^n_{i,\text{1st-PINN}} / EI_{i,\text{1st}}$	$P^n_{i,\text{2nd-PINN}} / P_{i,\text{2nd}}$
1[a]	7.00	1.43	0.0285618566	0.2048378740	2.59E-04	3.93E-04	**0.00**	**-0.69**
2[a]	7.01	1.31	0.0285173673	0.1878028806	4.13E-04	5.84E-04	**0.14**	**2.34**
3[a]	7.04	0.90	0.0283834506	0.1283070304	6.17E-04	9.97e-04	**0.57**	**-6.25**
4[b]	6.66	1.63	0.0300534852	0.2448170331	5.28E-04	6.22E-04	**0.15**	**1.88**
5[b]	6.30	1.58	0.0317363888	0.2500538828	1.11E-04	5.97E-04	**0.00**	**-1.25**
6[b]	5.61	1.64	0.0356790014	0.2934747642	2.80E-04	6.19E-04	**0.18**	**2.50**
7[c]	5.61	0.95	0.0356623381	0.1703697440	7.24E-04	5.23E-04	**0.18**	**-1.04**

The result demonstrates the computational feasibility of the sequential procedure but also reveals an important inverse-problem characteristic: accurate reproduction of the displacement field does not necessarily guarantee accurate recovery of a weakly influential physical parameter. In the present sequential case, the first-stage estimate δ_{1st}=0.0284968894, compared with the reference value δ_{1st}=0.0285714286, corresponds to a transferred rigidity bias of approximately 0.26%. When the identified n and the transferred rigidity are both back-substituted into Equation (7b), the corresponding prestress-force error is approximately 11.05%. The following subsection examines whether this amplification is consistent with the conditioning of the second-stage inverse problem.

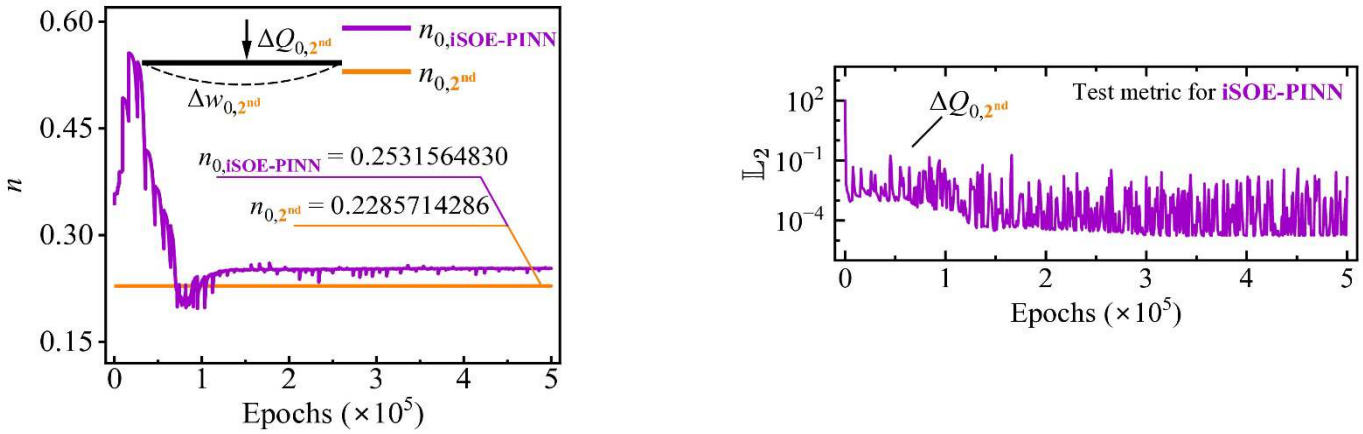

Figure 7 Representative sequential estimation using iSOE-PINN: (a) convergence of the nondimensional axial-force parameter n; (b) relative L2 displacement error.

Rigidity-transfer sensitivity and error propagation

To quantify the propagation of first-stage rigidity error independently of neural-network optimization, the second-stage inverse problem is first examined conditionally for a fixed observed displacement field. Let EI_tr denote the rigidity transferred from the first-order stage. The dimensional residual of the second-order governing equation is written as

$$r(x; EI_{tr}, P) = EI_{tr}\Delta w'' + P\cos\theta\Delta w + \frac{\Delta Q x}{2} \tag{23}$$

For a fixed displacement field Δw(x), the conditional least-squares functional is defined as

$$J(EI_{tr}, P) = \int_0^{L/2} r^2(x; EI_{tr}, P)\,dx \tag{24}$$

Imposing the stationary condition ∂J/∂P=0 gives

$$\hat{P}(EI_{\mathrm{tr}}) = -\frac{\int_0^{L/2} \Delta w\left(EI_{\mathrm{tr}}\Delta w'' + \frac{\Delta Q x}{2}\right)\cos\theta\, dx}{\int_0^{L/2} \cos^2\theta (\Delta w)^2\, dx} \tag{25}$$

Differentiating Equation (25) with respect to the transferred rigidity yields

$$\frac{\partial \hat{P}}{\partial EI_{\mathrm{tr}}} = -\frac{1}{\cos\theta}\frac{\int_0^{L/2} \Delta w \Delta w''\, dx}{\int_0^{L/2} (\Delta w)^2\, dx} \tag{26}$$

For the half-span boundary conditions Δw(0)=0 and Δw'(L/2)=0, integration by parts gives

$$\frac{\partial \hat{P}}{\partial EI_{\mathrm{tr}}} = \frac{1}{\cos\theta}\frac{\int_0^{L/2} (\Delta w')^2\, dx}{\int_0^{L/2} (\Delta w)^2\, dx} > 0 \tag{27}$$

A normalized rigidity-to-prestress amplification factor is therefore introduced as

$$A_{P,EI} = \frac{EI_{\mathrm{tr}}}{\hat{P}}\frac{\partial \hat{P}}{\partial EI_{\mathrm{tr}}} \tag{28}$$

This quantity measures the relative sensitivity of prestress-force recovery to a relative error in the transferred rigidity, as shown in Table 7. Because Equation (25) is linear in EI_{tr} for a fixed observed displacement field, the conditional error mapping is linear rather than merely a local first-order approximation. A numerical parameter sweep was then performed using the analytical second-order displacement field. The reference bending rigidity was 7.00×10^8 N m^2, the beam span was 10m, and the second-stage incremental load was 2.00×10^5 N. Four prestress-force levels represented in the numerical study were considered: 0.96, 1.28, 1.44 and 1.60 MN. The transferred rigidity was perturbed by -5%, -3%, -1%, +1%, +3%, and +5%. The resulting normalized amplification factors were 72.06, 54.04, 48.04 and 43.23 for prestress-force levels of 0.96, 1.28, 1.44 and 1.60 MN, respectively. Consequently, a 1% rigidity-transfer error corresponds to approximately 72.1%, 54.0%, 48.0% and 43.2% prestress-force error at the respective prestress levels. The amplification becomes larger as prestress force decreases, demonstrating that recovery of the axial-force contribution becomes increasingly ill-conditioned as the prestress-sensitive component of the displacement response becomes weaker.

For sufficiently large negative rigidity perturbations, the unconstrained conditional solution may leave the physically admissible prestress-force domain. Such values should not be interpreted as physically meaningful negative prestress; rather, they indicate a loss of identifiability when the transferred-rigidity discrepancy exceeds the information content carried by the weak second-order response. The representative sequential result provides an independent consistency check. The first-stage δ estimate corresponds to a transferred-rigidity error of approximately +0.26%. For P=1.60×10^{6}N, Equation (28) predicts a prestress-force error of approximately +11.31%, whereas back-substitution of the reported sequential n and transferred rigidity gives approximately +11.05%. The close agreement shows that the observed sequential bias is quantitatively consistent with rigidity-transfer amplification.

Table 7 Conditional mapping from transferred-rigidity error to prestress-force error.

P_{ref} (×10^{6}N)	$A_{P,EI}$	±1% *EI* error	±3% *EI* error	±5% *EI* error
0.96	72.06	±72.1%	±216.2%	±360.3%
1.28	54.04	±54.0%	±162.1%	±270.2%
1.44	48.04	±48.0%	±144.1%	±240.2%
1.60	43.23	±43.2%	±129.7%	±216.2%

Optimization stability under repeated initialization

The original representative sequential result was obtained from a single optimization trajectory and therefore cannot by itself distinguish systematic transfer amplification from stochastic optimization variability. To assess training stability, the independent and sequential inverse problems were repeated using N=10 neural network initialization seeds. Table 8 Statistical stability of the recovered parameters over ten repeated neural-network initializations. Values are reported as the sample mean, sample standard deviation, and 95% confidence interval of the mean.

For all repeated runs, the physical parameters, synthetic observations, collocation locations, measurement locations, loss weights, optimizer settings, and scalar-parameter initial guesses were held fixed. Only the neural-network initialization was varied. In addition, within each replicate, the independent and sequential 2nd-PINN models used the same paired initialization seed. This paired design reduces initialization-related confounding when assessing the additional error introduced by the transferred rigidity. For each recovered parameter, the sample mean, sample standard deviation, and 95% confidence interval were calculated. The 95% confidence interval of the mean was evaluated as

$$\bar{y} \pm t_{0.975,N-1} \frac{s}{\sqrt{N}} \tag{29}$$

where $\bar{y}$ is the sample mean, s is the sample standard deviation, and N=10.

The independent first-order runs yielded EI = (7.0147±0.0060)×10^{8}Nm^2, with a 95% confidence interval of [7.0104, 7.0190]×10^{8}Nm^2. The corresponding mean signed EI error was 0.210%±0.086%, with a 95% confidence interval of [0.148%, 0.272%]. The independent second-order runs yielded n = 0.228312±0.000617 and P = (1.5982±0.0043)×10^{6}N. The mean independent P error was -0.113%±0.270%, with a 95% confidence interval of [-0.305%, 0.080%]. The complete sequential framework yielded n = 0.252985±0.001684 and P = (1.7743±0.0130)×10^{6}N. The corresponding mean n error was 10.681%±0.737%, with a 95% confidence interval of [10.154%, 11.208%], while the mean P error was 10.894%±0.812%, with a 95% confidence interval of [10.313%, 11.475%]. The paired sequential P-error shift was 11.006±0.697 percentage points, with a 95% confidence interval of [10.508, 11.505] percentage points. This systematic shift is more than an order of magnitude larger than the run-to-run stochastic dispersion. The analytical sensitivity prediction of 11.31% also lies within the 95% confidence interval of the repeated sequential P errors. Therefore, the repeated-run results indicate that rigidity-transfer amplification is the dominant source of the representative sequential bias, whereas random initialization introduces only a comparatively small secondary variation. The mean relative L_2 displacement errors remained low, at 1.62×10^{-4} for the 1st-PINN, 1.15×10^{-4} for the independent 2nd-PINN, and 1.57×10^{-4} for the sequential 2nd-PINN.

Table 8 Statistical stability over N=10 repeated initializations

EI (×10^8 N m^2)	7.0147	0.0060	[7.0104, 7.0190]
EI error (%)	0.210	0.086	[0.148, 0.272]
Independent n	0.228312	0.000617	[0.227871, 0.228753]
Independent P (×10^6 N)	1.5982	0.0043	[1.5951, 1.6013]
Independent P error (%)	-0.113	0.270	[-0.305, 0.080]
Sequential n	0.252985	0.001684	[0.251780, 0.254190]
Sequential n error (%)	10.681	0.737	[10.154, 11.208]
Sequential P (×10^{6}N)	1.7743	0.0130	[1.7650, 1.7836]
Sequential P error (%)	10.894	0.812	[10.313, 11.475]
Sequential P-error shift (percentage points)	11.006	0.697	[10.508, 11.505]

5 Application to published experimental beam data and discussion

Data source and applicability conditions

The sequential framework is applied to deflection data reported in the published experiments of Bonopera et al (2018a). The source study investigated uncracked post-tensioned concrete beams under short-term static loading and used second-order deflection information for prestress-force estimation. Nine loading transitions are reconstructed from the tabulated measurements, as summarized in Table 9.

The present authors did not conduct the original experiment. The analysis therefore uses the published equilibrium deflection values rather than raw acquisition records. Detailed sensor calibration records, complete time histories, and direct measurements of support settlement or rotation were not available in the dataset used here. Consequently, this application is intended as a computational feasibility assessment using published measurements, rather than an independently controlled experimental or field validation.

Table 9 Parameters for nine experiments on prestressed concrete beams.

Cases	P^i (×10⁶N)	EI^i (×10⁸N·m²)	ΔQ (×10⁴N)	δ^i	π^i	Δw_1	Δw_2	Δw_3	Δw_4	Δw_5	Δw_6	Δw_7
						(mm)						
N_2-N_1	0.620	0.465	0.24	0.0149738	0.5843253	0.14	0.25	0.33	0.36	-	0.24	0.13
N_3-N_1	0.620	0.465	0.48	0.0299476	0.5843253	-0.03	0.37	0.50	0.59	-	0.34	0.20
N_3-N_2	0.617	0.465	0.24	0.0149738	0.5814980	-0.17	0.12	0.17	0.23	-	0.10	0.07
N_5-N_4	0.724	0.502	0.25	0.0144481	0.6320491	0.12	0.22	0.28	0.33	0.27	0.21	0.11
N_6-N_4	0.721	0.502	0.50	0.0288962	0.6294301	0.27	0.44	0.58	0.64	0.57	0.43	0.23
N_6-N_5	0.721	0.502	0.25	0.0144481	0.6294301	0.15	0.22	0.30	0.31	0.30	0.22	0.12
N_8-N_7	0.820	0.517	0.27	0.0151512	0.6950872	0.13	0.23	0.32	0.34	0.31	0.23	0.12
N_9-N_7	0.820	0.517	0.49	0.0274966	0.6950872	0.22	0.42	0.58	0.63	0.57	0.43	0.23
N_9-N_8	0.820	0.517	0.22	0.0123454	0.6950872	0.09	0.19	0.26	0.29	0.26	0.20	0.11

Identification results

Table 10 summarizes the estimates obtained for the nine loading transitions. The relative displacement errors range from approximately 2.9×10^{-5} to 4.4×10^{-4}, indicating close agreement between the predicted and tabulated deflection increments. The signed bending-rigidity errors range from approximately -3.3% to 3.3%. Most cases have an absolute error below 1.0%, although Cases N_3-N_1, N_6-N_4, and N_9-N_7 show larger deviations. These results indicate that the first-order stage provides comparatively consistent estimates of the first-order-equivalent rigidity for the considered dataset. Prestress-force estimation is substantially less accurate. The signed errors range from -39.2% to 29.5%. The three differences formed from adjacent loading stages, namely N_3-N_2, N_6-N_5, and N_8-N_7, produce underestimations of approximately 36.4%, 39.2%, and 20.1%, respectively. The larger-load differences N_3-N_1, N_6-N_4, and N_9-N_7 produce errors of approximately 11.9%, 10.1%, and 8.7%, respectively, while Case N_9-N_8 produces an overestimation of 29.5%.

The mechanical and measurement effects of load magnitude should be interpreted separately. Increasing the incremental load does not modify the nondimensional axial-force parameter or the normalized relative contribution of the second-order term in the adopted governing equation. Therefore, the comparatively smaller errors observed for several larger-load transitions cannot be interpreted as evidence of physical decoupling or intrinsic amplification of the prestress-force effect. A larger absolute deflection response may nevertheless improve the measurement signal-to-noise ratio if the sensor uncertainty has an approximately load-independent absolute magnitude. The available experimental dataset does not isolate this measurement effect from differences in loading transition, boundary behavior, and other structural conditions, and therefore does not support a general causal conclusion that increasing incremental load improves prestress-force identification.

More importantly, the contrast between the very small displacement errors and the substantially larger prestress-force errors illustrates the conditioning of the inverse problem. The global displacement response is dominated by flexural stiffness, whereas prestress force is inferred from the comparatively weak $P\Delta w$ contribution. A structural-model discrepancy that is negligible relative to the total displacement field may therefore be large relative to the response component carrying information about prestress force. Several unmodeled effects can produce this behavior. Minor support rotational stiffness or support friction changes the effective boundary conditions and curvature distribution; support settlement introduces displacement components absent from the ideal simply supported model; axial restraint modifies the effective axial-force state; shear deformation contributes additional displacement not represented by Euler-Bernoulli theory; and cross-sectional non-uniformity produces spatial variation in the effective bending rigidity. Because these effects are not represented explicitly in the present inverse model, part of their influence can be absorbed by the identified prestress-force parameter while the global displacement fit remains close to the measured response.

Consequently, displacement-field convergence is a necessary but insufficient condition for reliable inverse parameter identification. A low displacement error demonstrates compatibility of the reconstructed field with the observations, but it does not establish that a weakly influential physical parameter has been uniquely or accurately recovered.

The experimental prestress-force error range of -39.2% to 29.5% should therefore be interpreted as evidence of the current sensitivity to model and measurement discrepancy rather than as field-ready diagnostic accuracy.

Table 10. The identification results and percentage errors for the nine test cases.

Cases	$P^i_{\text{Identified}}$ (×10^{6}N)	$EI^i_{\text{Identified}}$ (×10^{8}N·m^2)	$\delta^i_{\text{Identified}}$	$n^i_{\text{Identified}}$	L_2	Error (%)	
						$P^i_{\text{Identified}} / P^i$	$EI^i_{\text{Identified}} / EI^i$
N_2-N_1	0.420	0.462	0.01508544	0.39853743	1.26E-04	**-32.3**	**-0.74**
N_3-N_1	0.694	0.478	0.02912626	0.63592691	5.30E-05	**11.9**	**2.82**
N_3-N_2	0.392	0.461	0.01511895	0.37341751	4.22E-04	**-36.4**	**-0.96**
N_5-N_4	0.517	0.507	0.01430928	0.44694768	4.13E-05	**-28.6**	**0.97**
N_6-N_4	0.794	0.519	0.02797035	0.67079912	5.21E-05	**10.1**	**3.31**
N_6-N_5	0.438	0.497	0.01458371	0.38628598	3.72E-04	**-39.2**	**-0.93**
N_8-N_7	0.655	0.512	0.01529807	0.56075795	4.43E-04	**-20.1**	**-0.96**
N_9-N_7	0.891	0.500	0.02842029	0.78094034	4.12E-05	**8.7**	**-3.25**
N_9-N_8	1.062	0.514	0.01240871	0.90475215	2.90E-05	**29.5**	**-0.51**

Interpretation, limitations, and future work

The main methodological value of the proposed framework is the reorganization of a coupled inverse problem into two conditional stages. This strategy reduces the number of simultaneously trainable physical parameters and provides a transparent route for transferring stiffness-related information into the prestress-force estimation stage. The new sensitivity analysis also shows that this transfer introduces an important conditioning problem: even a small first-stage rigidity bias can be strongly amplified in the recovered prestress force when the second-order contribution is weak. The method nevertheless has several important limitations.

6. The rigidity obtained from the first-order equation is a model-dependent equivalent quantity and is not guaranteed to equal the bending rigidity in the second-order structural representation. The analytical and numerical sensitivity results demonstrate that this distinction is not merely conceptual; it can have a quantitatively large effect on prestress-force recovery.
7. Changing the incremental-load magnitude does not change the nondimensional axial-force parameter in the adopted linear model. A larger load can improve measurement observability only when the absolute measurement-noise floor remains approximately fixed. Such an SNR benefit is a measurement effect and should not be interpreted as mechanical decoupling.
8. The current formulation assumes a slender, uncracked Euler-Bernoulli beam with ideal simply supported boundary conditions. Shear deformation, minor support rotational stiffness, support friction or settlement, axial restraint, cracking, material nonlinearity, tendon slip, cross-sectional non-uniformity, and three-dimensional structural behavior are not included. Because prestress force is inferred from a weak second-order response contribution, these effects may disproportionately bias the recovered prestress force while producing only small changes in the total displacement field.
9. The experimental application is reconstructed from a published laboratory dataset. Raw sensor records, detailed calibration information, and independently measured boundary-condition data were not available for uncertainty propagation. The present results therefore do not establish field robustness.
10. Direct quantitative comparison with other prestress-force identification methods remains limited by differences in structural configuration, loading type, sensor arrangement, unknown parameters, and error definitions. The literature discussion in the Introduction is therefore intended as a methodological comparison rather than a quantitative performance ranking.

The present framework should accordingly be interpreted as a preliminary baseline tool for sequential physics-informed inverse analysis rather than a field-ready diagnostic. Future work should investigate explicit boundary-condition uncertainty, support-displacement measurements, spatial stiffness variability, physically admissible parameter constraints, uncertainty propagation, and extensions to Timoshenko and nonlinear beam formulations. The dependence of repeated-run statistics on network architecture and optimization settings should also be examined. Independent tests on additional prestressed concrete beams and bridge girders remain necessary before reliable field application can be claimed.

6 Conclusions

This study investigated an incremental second-order-effect-guided PINN framework for sequential estimation of bending rigidity and prestress force in prestressed concrete beams. The main conclusions are as follows.

11. The coupled bending-rigidity and prestress-force inverse problem can be reorganized into two conditional stages. The first-order PINN estimates a first-order-equivalent rigidity, and the second-order PINN estimates the nondimensional axial-force parameter conditional on the transferred rigidity. The procedure reduces the number of simultaneously unknown parameters but does not constitute exact physical decoupling.

12. In the adopted linear incremental model, changing the incremental load scales the absolute deflection response but does not change the nondimensional axial-force parameter or the normalized relative contribution of the second-order term. Any benefit of a larger load should therefore be interpreted as improved measurement observability under an approximately fixed absolute noise floor rather than intrinsic amplification of the normalized second-order effect.

13. Independent numerical tests verify that the first- and second-order PINN models can reproduce their corresponding governing equations and identify a single unknown parameter. Under 1% Gaussian noise, the maximum absolute errors in the considered independent tests are approximately 0.6% for bending rigidity and 6.3% for prestress force. These values characterize the individual models and should not be interpreted as the accuracy of the complete sequential procedure.

14. The conditional sensitivity analysis demonstrates that prestress-force recovery can strongly amplify a small error in the transferred rigidity. For the considered prestress levels of 0.96-1.60 MN, the normalized rigidity-to-prestress amplification factor decreases from approximately 72.1 to 43.2 as prestress force increases. In the representative sequential case, a transferred-rigidity error of approximately 0.2616% predicts a prestress-force error of approximately 11.31%, in close agreement with the approximately 11.05% error obtained by back-substitution of the sequential solution. This agreement quantitatively confirms the importance of rigidity-transfer conditioning.

15. Repeated random-initialization tests confirm that the representative sequential bias is statistically stable. Across N=10 runs, the complete sequential framework yielded a mean prestress-force error of 10.894% with a standard deviation of 0.812 percentage points and a 95% confidence interval of [10.313%, 11.475%]. The paired sequential-minus-independent error shift was 11.006±0.697 percentage points, whereas the independent prestress-force error remained centered near zero at -0.113%±0.270%. The analytical prediction of 11.31% lies within the 95% confidence interval of the repeated sequential results. These results indicate that rigidity-transfer amplification, rather than stochastic initialization, is the dominant source of the approximately 11% sequential bias.

16. Application to nine loading transitions reconstructed from published experimental data yields signed errors of approximately -3.3% to 3.3% for bending rigidity and -39.2% to 29.5% for prestress force. The much larger prestress-force errors despite small displacement-field errors demonstrate that displacement convergence is necessary but insufficient for reliable recovery of a weakly influential physical parameter. Minor boundary-condition, shear-deformation, axial-restraint, and stiffness-distribution discrepancies can be small relative to the total displacement response while remaining large relative to the prestress-sensitive second-order component.

Overall, the proposed framework provides a transparent preliminary baseline for sequential physics-informed estimation. Its present applicability is limited to slender, uncracked, simply supported beams for which shear deformation, boundary-condition uncertainty, axial restraint, spatial stiffness variation, and material nonlinearity are negligible. Additional controlled experiments, explicit uncertainty propagation, and higher-order beam formulations are required before reliable field application can be established.

Acknowledgments

This research was funded by Key Research Project of Henan Provincial Universities (Grant No. 25B560015), and Joint Fund Project under Henan Provincial Science and Technology Research and Development Program (Grant No. 252103810025). The authors greatly appreciate these financial supports.

Author's Contributions: Conceptualization, Zhanguo Xia and Hong Zhang; methodology, Zhanguo Xia and Hong Zhang; software, Zhanguo Xia and Hong Zhang; validation, Zhanguo Xia; formal analysis, Hong Zhang; data curation, Junkui Pan; writing—original draft preparation, Zhanguo Xia; writing—review and editing, Junkui Pan; visualization, Hong Zhang; supervision, Junkui Pan; project administration, Junkui Pan; funding acquisition, Junkui Pan. All authors have read and agreed to the published version of the manuscript.

Data availability statement: The numerical parameter settings and tabulated results analyzed in this study are provided in the article. Synthetic reference observations can be regenerated from the analytical solutions and parameter settings reported in the manuscript. The numerical data generated for the rigidity-transfer sensitivity analysis and repeated-initialization study. The experimental deflection data were reconstructed from the cited published source. No new experimental dataset was generated in this study.

Editor: Rogério José Marczak.

References

Abdel-Jaber, H., Glisic, B., (2019). Monitoring of prestressing forces in prestressed concrete structures—An overview. Structural Control and Health Monitoring 26:e2374.

Abdolrasol, M.G.M., Hussain, S.M.S., Ustun, T.S., Sarker, M.R., Hannan, M.A., Mohamed, R., Ali, J.A., Mekhilef, S., Milad, A., (2021). Artificial neural networks based optimization techniques: A review. Electronics 10:2689.

Abdulkadirov, R., Lyakhov, P., Nagornov, N., (2023). Survey of optimization algorithms in modern neural networks. Mathematics 11:2466.

Antonion, K., Wang, X., Raissi, M., Joshie, L., (2024). Machine learning through physics-informed neural networks: Progress and challenges. Academic Journal of Science and Technology 9:46–49.

Bonopera, M., Chang, K.C., Chen, C.C., Sung, Y.C., Tullini, N., (2018a). Feasibility study of prestress force prediction for concrete beams using second-order deflections. International Journal of Structural Stability and Dynamics 18:1850124.

Bonopera, M., Chang, K.C., Chen, C.C., Sung, Y.C., Tullini, N., (2018b). Prestress force effect on fundamental frequency and deflection shape of PCI beams. Structural Engineering and Mechanics 67:255–265.

Breccolotti, M., (2018). On the evaluation of prestress loss in PRC beams by means of dynamic techniques. International Journal of Concrete Structures and Materials 12:1.

Chiu, P.H., Wong, J.C., Ooi, C., Dao, M.H., Ong, Y.S., (2022). CAN-PINN: A fast physics-informed neural network based on coupled automatic–numerical differentiation method. Computer Methods in Applied Mechanics and Engineering 395:114909.

Cornaggia, A., Garbowski, T., Cocchetti, G., Ferrari, R., Rizzi, E., (2023). Optimised structural modelling for inverse analysis parameter identification relying on dynamic measurements. Proceedings of the 9th International Conference on Computational Methods in Structural Dynamics and Earthquake Engineering (COMPDYN 2023):4234–4248.

da Silva, A.R., de Souza Rosa, J.P., (2020). Nonlinear numerical analysis of prestressed concrete beams and slabs. Engineering Structures 223:111187.

Dolan, C.W., Hamilton, H.R., (2019). Prestressed concrete: Building, design, and construction, Springer Cham.

Guo, T., Chen, Z., Lu, S., Yao, R., (2018). Monitoring and analysis of long-term prestress losses in post-tensioned concrete beams. Measurement 122:573–581.

Huth, O., Feltrin, G., Maeck, J., Kilic, N., Motavalli, M., (2005). Damage identification using modal data: Experiences on a prestressed concrete bridge. Journal of Structural Engineering 131:1898–1910.

Jeyamohan, K., Chan, T.H., Nguyen, K.D., Thambiratnam, D.P., (2025). Prestress force and moving force identification in prestressed concrete bridges via Lagrangian polynomial-based load shape function approach. Journal of Civil Structural Health Monitoring 15:575–596.

Jia, J., Zhang, L., Ou, J., Chen, X., (2023). Nondestructive testing and health monitoring techniques for structural effective prestress. Structural Control and Health Monitoring 2023:8940008.

Krishnapriyan, A., Gholami, A., Zhe, S., Kirby, R., Mahoney, M.W., (2021). Characterizing possible failure modes in physics-informed neural networks. Advances in Neural Information Processing Systems 34:26548–26560.

Lawal, Z.K., Yassin, H., Lai, D.T.C., Che Idris, A., (2022). Physics-informed neural network evolution and beyond: A systematic literature review and bibliometric analysis. Big Data and Cognitive Computing 6:140.

Meng, Z., Qian, Q., Xu, M., Yu, B., Yıldız, A.R., Mirjalili, S., (2023). PINN-FORM: A new physics-informed neural network for reliability analysis with partial differential equation. Computer Methods in Applied Mechanics and Engineering 414:116172.

Pang, G., Lu, L., Karniadakis, G.E., (2019). fPINNs: Fractional physics-informed neural networks. SIAM Journal on Scientific Computing 41:A2603–A2626.

Raissi, M., Perdikaris, P., Karniadakis, G.E., (2019). Physics-informed neural networks: A deep learning framework for solving forward and inverse problems involving nonlinear partial differential equations. Journal of Computational Physics 378:686–707.

Schommer, S., (2017). Damage detection in prestressed concrete bridges based on static load testing, sagging and modal parameters, using measurements and model updating, Ph.D. Thesis, University of Luxembourg, Luxembourg.

Teloli, R.O., Tittarelli, R., Bigot, M., Coelho, L., Ramasso, E., Le Moal, P., Ouisse, M., (2025). A physics-informed neural networks framework for model parameter identification of beam-like structures. Mechanical Systems and Signal Processing 224:112189.

Toscano, J.D., Oommen, V., Varghese, A.J., Zou, Z., Ahmadi Daryakenari, N., Wu, C., Karniadakis, G.E., (2025). From PINNs to PIKANs: Recent advances in physics-informed machine learning. Machine Learning for Computational Science and Engineering 1:15.

Xie, L., Wang, S., Ding, J., Banerjee, J.R., Wang, J., (2020). An accurate beam theory and its first-order approximation in free vibration analysis. Journal of Sound and Vibration 485:115567.

Yang, Y., Guo, Z., Liu, Z., (2025). Parameter identification in prestressed concrete beams by incremental beam–column equation and physics-informed neural networks. Computer-Aided Civil and Infrastructure Engineering 40:2876–2899.

Yapar, O., Basu, P.K., Nordendale, N., (2015). Accurate finite element modeling of pretensioned prestressed concrete beams. Engineering Structures 101:163–178.

Yu, Q.Q., Gu, X.L., Zeng, Y.H., Zhang, W.P., (2022). Flexural behavior of corrosion-damaged prestressed concrete beams. Engineering Structures 272:114985.

Zhang, X.S., (2013). Neural networks in optimization, Vol. 46, Springer Science & Business Media.